

# Analytical and Experimental Investigation on the Magnetic Field and Torque of a Permanent Magnet Spherical Actuator

Liang Yan, I-Ming Chen, *Senior Member, IEEE*, Guilin Yang, *Member, IEEE*, and Kok-Meng Lee, *Fellow, IEEE*

**Abstract**—This paper presents the torque model of a ball-joint-like three-degree-of-freedom (3-DOF) permanent magnet (PM) spherical actuator. This actuator features a ball-shaped rotor with multiple PM poles and a spherical stator with circumferential air-core coils. An analytical expression of the magnetic field of the rotor is obtained based on Laplace's equation. Based on this expression and properties of air-core stator coils, Lorentz force law is employed for the study of the relationship between the rotor torque and coil input currents. By using linear superposition, the expression of the actuator torque in terms of current input to the stator coils can be obtained in a matrix form. The linear expression of the actuator torque will facilitate real-time motion control of the actuator as a servo system. Experimental works are carried out to measure the actual magnetic field distribution of the PM rotor in three-dimensional (3-D) space as well as to measure the actual 3-D motor torque generated by the actuator coils. The measurement results were coincident with analytical study on the rotor magnetic field distribution and actuator torque expressions. The linearity and superposition of the actuator torque were also verified through the experiments.

**Index Terms**—Magnetic field, spherical actuator, torque model.

## I. INTRODUCTION

CONVENTIONALLY, a three-degree-of-freedom (3-DOF) spherical motion can be realized by several single-axis actuators connected in parallel or in series. Such a spherical motion-generating device inherently has bulky structure, large backlash, and motion singularities. In applications requiring compact multi-DOF spherical motion, a spherical actuator with a ball-joint-like device that can produce 2- or 3-DOF rotational motion is desired. Unlike single-axis actuators, the torque output of the spherical actuator has three components. Because all torque components are dependant on rotor orientation, to obtain actuator torque in terms of input current to the motor coils becomes a complicated problem.

Manuscript received October 31, 2005; revised April 2, 2006. Recommended by Guest Editors K. M. Lee and S. Chiaverini. This work was supported by a collaborative research project under Grant U02-A-O40B for Nanyang Technological University, Singapore Institute of Manufacturing Technology, and Georgia Institute of Technology.

L. Yan and I-M. Chen are with the School of Mechanical and Aerospace Engineering, Nanyang Technological University, Singapore 637098 (e-mail: yanliang@pmail.ntu.edu.sg; michen@ntu.edu.sg).

G. Yang is with Mechatronics Group, Singapore Institute of Manufacturing Technology, Singapore 638075 (e-mail: glyang@simtech.a-star.edu.sg).

K.-M. Lee is with George W. Woodruff School of Mechanical Engineering, Georgia Institute of Technology, Atlanta, GA 30332-0405 USA (e-mail: kokmeng.lee@me.gatech.edu).

Digital Object Identifier 10.1109/TMECH.2006.878545

Williams *et al.* [1] have designed the first spherical induction motor to obtain a variable-speed drive of a single-axis ac motor based on relative inclination of the rotating shaft. The magnetic field generated by the stator windings induces current on the rotor surface, and causes the rotor to incline. Davey *et al.* [2] derived the torque model of this induction motor by integrating the Maxwell stress moment over the spherical rotor surface and proposed its use as a robot wrist [3]. The mechanical complexity and the inherent poor servo characteristics of the spherical induction motor led Lee and Kwan [4] to develop a 3-DOF spherical stepper based on the principle of variable reluctance, which takes advantage of the high coercivity of modern rare-earth permanent magnets (PMs). The torque output of a variable-reluctance spherical motor (VRSM) depends on the current inputs as well as the magnetic reluctance at the air gaps between the rotor and the stator poles [5]. For any attainable rotor orientation, optimal current inputs [6], [7] can be found to move the rotor to a neighborhood with knowledge of reluctance. The torque model of this motor is obtained by differentiating coenergy with respect to the angular displacement parameters. In the past decade, several variations of spherical motors with a structure similar to [4] have been studied. Wang *et al.* [8]–[11] have developed spherical actuators achieving 2-/3-DOF motions. The rotor is a completely magnetized ball. Coils are uniformly mounted on the stator. The torque models of these spherical actuators were obtained by using Lorentz force law. Chirikjian and Stein [12] have made a spherical stepper with a PM-pole rotor and a stator with an array of coils. Difference in the symmetric layout of the rotor poles and the stator poles allows stepping motion in three orientations. Commutation of this stepper motor has been studied to move the rotor. Kahlen *et al.* [13] developed a spherical motor consisting of a rotor sphere with 112 PM poles and an outer stator with 96 stator windings. The poles were arranged symmetrically corresponding to lines of longitude and latitude of a globe. The force/torque produced by the stator winding was calculated numerically. More recently, Lee *et al.* [14], [15] have developed a spherical wheel motor (SWM) that offers a means to control the orientation of its rotating shaft in an open-loop fashion.

This article offers an alternative analytical expression for computing the torque output of a spherical actuator that consists of a ball-shaped rotor with a full circle of PM poles and a spherical-shell-like stator with multiple layers of air-core coils [16], [17]. This configuration allows more PM poles and coils incorporated to increase the motion resolution and working range of the actuator. Based on Laplace equation and

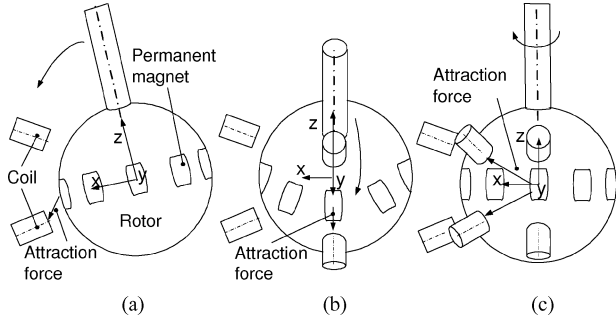


Fig. 1. 3-DOF motion of the spherical actuator. (a) First tilting motion. (b) Second tilting motion. (c) Spinning motion.

suitable boundary conditions, the distribution of magnetic field surrounding the rotor can be obtained analytically. Due to the use of air-core coils, Lorentz force law can be used for the derivation of the relationship between the actuator torque and input coil currents. The complete actuator torque can be expressed in a matrix form in terms of input currents from all coils through linear superposition. This analytical expression of the torque output can be used for motion control and design optimization of the spherical actuator. Experimental verification of the three-dimensional (3-D) magnetic field surrounding the rotor and 3-D actuator torques was carried out. The tasks included the design and installation of a semiautomatic 3-D magnetic field measurement system and 3-D torque measurement testbed, measurement data acquisition and processing. Comparisons between analytical and experimental data show feasibility and consistency of the proposed magnetic field model of the rotor and torque model although there are minor errors which may be due to the omission of higher order harmonics.

## II. WORKING PRINCIPLE

The working principle of the spherical actuator is illustrated in Fig. 1. The rare-earth PMs (NdFeB) mounted along the rotor equator can produce high flux density. The air-core coils are assembled on the stator, which can simplify the torque model of the spherical actuator in a linear fashion. By activating pairs of coils in two longitudinal directions, the rotor can tilt in two orthogonal directions as shown in Fig. 1(a) and (b). Energizing all circumferential coils, the rotor can spin about its own axis [Fig. 1(c)]. Therefore, by varying the input currents of the coils, any desirable 3-DOF spherical motion within the workspace can be achieved.

## III. FORMULATION OF THE MAGNETIC FIELD

In formulating the magnetic field of the rotor, we use a generic rotor model shown in Fig. 2 for discussion. The PM rotor poles are evenly spaced (with alternate polarities) around the rotor equator, each of which has the shape of a dihedral cone defined in terms of four parameters: longitudinal angle  $\alpha$ , latitudinal angle  $\beta$ , and outer and inner radii  $R_r$  and  $R_b$ . With such an arrangement, the study of the rotor magnetic field can be divided into three parts.

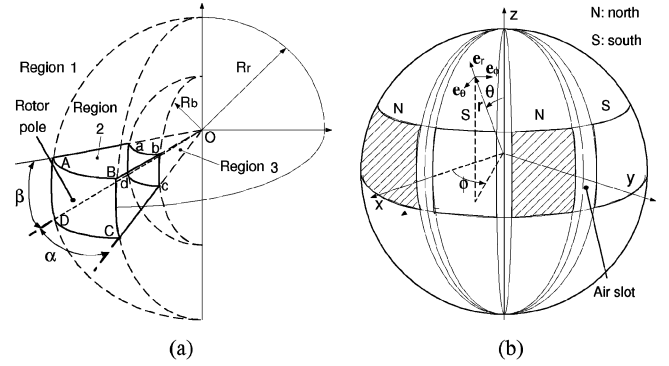


Fig. 2. Arrangement of rotor poles. (a) Single rotor pole. (b) Alternately arranged poles.

1) *Air Space Outside the Rotor (Region 1)*: The magnetic effect of air space can be characterized by

$$\mathbf{B}_1 = \mu_0 \mathbf{H}_1 \quad (1)$$

where the subscript "1" denotes Region 1;  $\mathbf{B}$  and  $\mathbf{H}$  are the magnetic flux density and field intensity; and  $\mu_0$  is the permeability of the free space with a value of  $4\pi \times 10^{-7}$  H/m.

2) *Within the Dihedral PM Rotor Poles (Region 2)*: The magnetic property of PM can be represented by

$$\mathbf{B}_2 = \mu_0 \mu_m \mathbf{H}_2 + \mu_0 \mathbf{M}_0 \quad (2)$$

where  $\mu_m$  is the dimensionless relative recoil permeability of PM (typical value ranging between 1.05 and 1.20);  $\mathbf{M}_0 = \mathbf{B}_{\text{rem}}/\mu_0$  is the residual magnetization vector in Ampere per meter; and  $\mathbf{B}_{\text{rem}}$  is defined as the remanence in Tesla. In spherical coordinates, the residual magnetization vector of the  $p^{\text{th}}$  PM can be expressed as

$$\mathbf{M}_0 = \begin{bmatrix} M_{0r} \\ M_{0\theta} \\ M_{0\phi} \end{bmatrix} = (-1)^{p-1} |\mathbf{M}_0| \begin{bmatrix} \cos(\phi - \alpha_p) \sin \theta \\ \cos(\phi - \alpha_p) \cos \theta \\ -\sin(\phi - \alpha_p) \end{bmatrix} \quad (3)$$

where  $\alpha_p = \alpha/2 + 2\pi(p-1)/P$ ,  $p = 1, 2, \dots, P$ .  $P$  is the total number of PM poles. In this study, let  $P = 8$ . Note that these equations are only valid within the range of

$$0 < \phi - \frac{2\pi(p-1)}{P} < \alpha, \quad \frac{\pi}{2} - \frac{\beta}{2} < \theta < \frac{\pi}{2} + \frac{\beta}{2}.$$

For the nonmagnetized space in between poles on the rotor, the residual magnetization is equal to zero.

3) *Rotor Core Made of Ferromagnetic Material (Region 3)*: The magnetic property of ferromagnetic material such as soft iron should be

$$\mathbf{B}_3 = \mu_0 \mu_r \mathbf{H}_3 \quad (4)$$

where  $\mu_r$  is the relative permeability of the ferromagnetic core (typically larger than 4000).

### A. Governing Equations

The Maxwell's equations that govern the magnetic field distribution of the spherical rotor are formulated using scalar potential

function. For an irrotational magnetic field

$$\nabla \times \mathbf{H} = 0, \quad \nabla \cdot \mathbf{B} = 0 \quad (5)$$

where  $\mathbf{H}$  is curl free and can be expressed in terms of a scalar potential function  $\Phi$  based on Helmholtz's theorem as

$$\mathbf{H} = -\nabla\Phi. \quad (6)$$

In the spherical coordinates

$$\begin{aligned} \mathbf{H} &= H_r \mathbf{e}_r + H_\theta \mathbf{e}_\theta + H_\phi \mathbf{e}_\phi \\ &= \left[ -\frac{\partial\Phi}{\partial r}, -\frac{1}{r} \frac{\partial\Phi}{\partial\theta}, -\frac{1}{r \sin\theta} \frac{\partial\Phi}{\partial\phi} \right]^T \end{aligned} \quad (7)$$

where  $\mathbf{e}_r$ ,  $\mathbf{e}_\theta$ , and  $\mathbf{e}_\phi$  are the respective unit vectors; and  $H_r$ ,  $H_\theta$ , and  $H_\phi$  are components of the magnetic field intensity.

For Regions 1 and 3, the scalar potentials are governed by the Laplace equations

$$\nabla^2\Phi_1 = 0, \quad \nabla^2\Phi_3 = 0. \quad (8)$$

Based on (2), (5), and (6), the scalar potential  $\Phi_2$  within PM pole (Region 2) can be expressed as

$$\nabla^2\Phi_2 = \nabla \cdot \frac{\mathbf{M}_0}{\mu_m} \quad (9)$$

which is in the form of Poisson's equation. With a symmetric arrangement of rotor poles, the divergence of the residual magnetization vector is equal to zero, i.e.,  $\nabla \cdot \mathbf{M}_0 = 0$ . Thus, the Poisson's equation can be reduced to Laplace's equation,  $\nabla^2\Phi_2 = 0$ . Once the Laplace's equations of all three regions are solved, the magnetic intensity can be obtained. Consequently, the flux density can be solved analytically. The analytical expression of flux density can be used for the torque computation based on Lorentz force law.

### B. General Solution to Laplace's Equations

The Laplace's equation can be written in spherical coordinates as

$$\frac{1}{r^2} \left[ \frac{\partial}{\partial r} (r^2 \Phi_i) + \frac{1}{\sin\theta} \frac{\partial}{\partial\theta} \left( \sin\theta \frac{\partial\Phi_i}{\partial\theta} \right) + \frac{1}{\sin^2\theta} \frac{\partial\Phi_i}{\partial\phi} \right] = 0 \quad (10)$$

where  $i$  ( $= 1, 2$ , and  $3$ ) denotes the region of concern. Based on the separation of variables, i.e.,  $\Phi_i(r, \theta, \phi) = R_i(r)\Theta_i(\theta)\Psi_i(\phi)$ , where  $R_i(r)$ ,  $\Theta_i(\theta)$ , and  $\Psi_i(\phi)$  are independent functions, the general solution to the Laplace equations characterizing all three regions has the following form:

$$\Phi_i = \sum_{n=0}^{\infty} \sum_{m=-n}^n \left( \kappa_{n,i}^m r^n + \xi_{n,i}^m r^{-(n+1)} \right) Y_n^m(\theta, \phi) \quad (11)$$

where  $\kappa_{n,i}^m$  and  $\xi_{n,i}^m$  are constants to be determined by the boundary conditions. The angular part of the solutions to the Laplace's equation  $Y_n^m$  is a complex-valued spherical harmonic function defined by

$$Y_n^m(\theta, \phi) = S_n^m P_n^m(\cos\theta) e^{im\phi}$$

where

$$S_n^m = \sqrt{\frac{2n+1}{4\pi} \frac{(n-m)!}{(n+m)!}}$$

$P_n^m(\cos\theta)$  is associated Legendre functions; and  $n$  and  $m$  are integers with the condition  $-n \leq m \leq n$ .

### C. Boundary Conditions

The particular solutions that characterize the magnetic scalar potentials of three regions require the specification of the source term and the six unknowns,  $\kappa_{n,i}^m$  and  $\xi_{n,i}^m$ , where  $i = 1, 2$ , and  $3$ . These unknowns can be solved from the following boundary conditions.

1) *Boundary Condition at the Far Field*: The magnetic flux density approaches zero when  $r \rightarrow \infty$ , i.e.,  $\mathbf{B}_1|_{r \rightarrow \infty} = 0$ . This boundary condition implies

$$B_{1r}|_{r \rightarrow \infty} = -\mu_0 \frac{\partial\Phi_1}{\partial r} \Big|_{r \rightarrow \infty} = 0$$

or

$$\begin{aligned} -\mu_0 \sum_{n=0}^{\infty} \sum_{m=-n}^n \left( n \kappa_{n,1}^m r^{n-1} - (n+1) \xi_{n,1}^m r^{-(n+2)} \right) Y_n^m \\ \times (\theta, \phi) \Big|_{r \rightarrow \infty} = 0. \end{aligned}$$

Through inspection of the exponential terms, it can be concluded that  $\kappa_{n,1}^m = 0$ . From (7) and (11), it can be verified that the boundary conditions  $B_{1\theta}|_{r \rightarrow \infty} = 0$  and  $B_{1\phi}|_{r \rightarrow \infty} = 0$  yield the same result.

2) *Finite Boundary Condition at  $r = 0$* : The flux density at  $r = 0$  must be finite, which implies that  $\mathbf{B}_3|_{r=0} \neq \infty$ . According to (7) and (11), the boundary condition  $B_{3r}|_{r=0} \neq \infty$  can be written as

$$B_{3r}|_{r=0} = -\mu_0 \frac{\partial\Phi_3}{\partial r} \Big|_{r=0} \neq \infty.$$

From this equation, it can be verified that  $\xi_{n,3}^m = 0$ .  $B_{3\theta}|_{r=0} \neq \infty$  and  $B_{3\phi}|_{r=0} \neq \infty$  yield the same result.

3) *Continuity at the Interface Between Two Different Media*: At the boundary of different regions (in between Regions 1 and 2, or Regions 2 and 3) shown in Fig. 3(a), the radial components of the flux density normal to the interfacial surface must be continuous. Additionally, Ampere's circuital law states that the line integral of the magnetic intensity along any closed contour is always equal to the real total current crossing a surface limited by the contour. As illustrated in Fig. 3(b), along the narrow rectangular contour  $abcd$  at the boundary surface, where the length segments  $l_{da}$  and  $l_{bc}$  are very small such that  $l_{cd} = l_{ab}$ , there is no real surface currents on the boundary. Hence

$$H_{2t} l_{cd} - H_{1t} l_{ab} = 0, \quad \text{or } H_{2t} = H_{1t}$$

where  $H_{1t}$  and  $H_{2t}$  are tangent to the surface. For the spherical actuator, there are two components  $H_\theta$  and  $H_\phi$  of the magnetic field intensity that are tangent to the rotor surface. The two boundary conditions shown in Fig. 3 at the interface of the air and PM (Regions 1 and 2) as well as the PM and soft iron (Regions 2 and 3) are stated as follows.

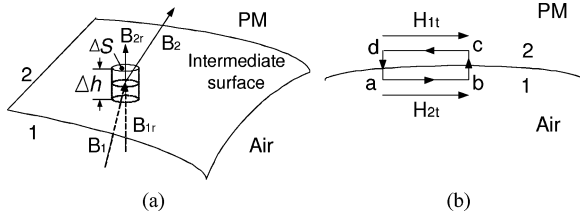


Fig. 3. Continuity of boundary conditions. (a)  $B_{1r} = B_{2r}$ . (b)  $H_{1t} = H_{2t}$ .

At the air and PM boundary

$$B_{1r}|_{r=R_r} = B_{2r}|_{r=R_r} \quad (12)$$

$$H_{1\phi}|_{r=R_r} = H_{2\phi}|_{r=R_r} \quad \text{and}$$

$$H_{1\theta}|_{r=R_r} = H_{2\theta}|_{r=R_r}. \quad (13)$$

At the PM and soft iron boundary

$$B_{2r}|_{r=R_b} = B_{3r}|_{r=R_b} \quad (14)$$

$$H_{2\phi}|_{r=R_b} = H_{3\phi}|_{r=R_b} \quad \text{and}$$

$$H_{2\theta}|_{r=R_b} = H_{3\theta}|_{r=R_b}. \quad (15)$$

#### D. Solution of Scalar Potential and Flux Density

To utilize the continuity on the boundary conditions between two medians, the radial component of residual magnetization vector needs to be expanded in spherical harmonics.

1) *Spherical Harmonic Expansion of  $M_{0r}$* : The radial component of the residual magnetization vector  $M_{0r}$  can be expressed as an expansion of spherical harmonic functions  $Y_n^m(\theta, \phi)$  as

$$M_{0r}^s(\theta, \phi) = \sum_{n=0}^{\infty} \sum_{m=-n}^n C_{n,m} Y_n^m(\theta, \phi) \quad (16)$$

where  $C_{n,m}$  are coefficients determined from the surface integral of the following form:

$$C_{n,m} = \int_0^\pi \int_0^{2\pi} M_{0r}(\theta, \phi) [Y_n^{m*}(\theta, \phi)] \sin \theta d\theta d\phi \quad (17)$$

and  $Y_n^{m*}(\theta, \phi)$  denotes the complex conjugate of  $Y_n^m(\theta, \phi)$ . Substituting (3) into (17) gives the coefficients

$$C_{n,m} = |\mathbf{M}_0| \int_0^{2\pi} f(\phi) e^{im\phi} d\phi \int_0^\pi S_n^m P_n^m(\cos \theta) \sin^2 \theta d\theta \quad (18)$$

where  $f(\phi) = (-1)^{p-1} \cos(\phi - \alpha_p)$ ,  $p = 1, 2, \dots, 8$ . Hence,  $C_{n,m} \neq 0$  if and only if  $m = \pm 4, \pm 12, \pm 20, \dots$ . Thus, the fundamental terms of the spherical harmonic functions can be taken at  $n = 4$  and  $m = \pm 4$ . Because the influence of fundamental terms is crucial, higher order terms are omitted in the derivation of the magnetic field

$$C_{4,\pm 4} = |\mathbf{M}_0| \frac{c}{\sqrt{\pi}} (a \pm bi) \quad (19)$$

where  $a$ ,  $b$ , and  $c$  are real numbers given by

$$a \pm bi \equiv \int_0^{2\pi} f(\phi) e^{im\phi} d\phi \quad (m = \pm 4)$$

$$\frac{c}{\sqrt{\pi}} \equiv \int_0^\pi S_n^m \sin^2 \theta [P_n^m(\cos \theta)] d\theta.$$

It can be verified that the results of the second integral for  $m = 4$  and  $m = -4$  are the same, and thus,  $C_{4,\pm 4}$  is a complex conjugate pair. Ultimately, the radial component  $M_{0r}$  of the residual magnetization vector can be expressed in terms of spherical harmonics as

$$M_{0r}^s(\theta, \phi) = C_{4,-4} Y_4^{-4}(\theta, \phi) + C_{4,4} Y_4^4(\theta, \phi) \quad (20)$$

where  $Y_4^{\pm 4} = \frac{3}{16} \sqrt{\frac{35}{2\pi}} \sin^4 \theta e^{\pm 4i\phi}$ .

2) *Derivation of the Coefficients*: The four boundary conditions on continuity can be further employed to derive the coefficients  $\xi_{n,i}^m$  and  $\kappa_{n,i}^m$  ( $i = 1, 2, 3$ ) by using the spherical harmonic expansion of  $M_{0r}$ . As the stator coils are situated in the free space outside of the rotor PM, the derivation of the scale potential and flux density is performed in Region 1. Therefore, only  $\xi_{n,1}^m$  and  $\kappa_{n,1}^m$  are concerned. Note that as shown in the boundary condition at far field  $\kappa_{n,1}^m = 0$ .

Utilizing (16), the radial component of  $\mathbf{B}_2$  can be expressed as

$$B_{2r} = \mu_m H_{2r} + \mu_0 \sum_{n=0}^{\infty} \sum_{m=-n}^n C_{n,m} Y_n^m(\theta, \phi). \quad (21)$$

From (7), (11), (21), and boundary conditions in (12)–(15), coefficient  $\xi_{n,1}^m$  can be obtained

$$\xi_{n,1}^m = -C_{n,m} d_n = -C_{n,m} d_n^\top / d_n^\perp \quad (22)$$

where

$$d_n^\top = R_r^{n+2} + \frac{\mu_m (2n+1) R_b^{n+2} R_r^{2n+1}}{(\mu_r - \mu_m) n R_b^{2n+1} - [\mu_r n + \mu_m (n+1)] R_r^{2n+1}}$$

$$d_n^\perp = (\mu_m - 1)(n+1) + \frac{\mu_m (2n+1) [\mu_r n + \mu_m (n+1)] R_r^{2n+1}}{(\mu_r - \mu_m) n R_b^{2n+1} - [\mu_r n + \mu_m (n+1)] R_r^{2n+1}}.$$

Particularly, for  $n = 4$  and  $m = \pm 4$ , coefficients of  $\xi_{4,1}^4$  and  $\xi_{4,1}^{-4}$  can be expressed with  $C_{4,4}$  and  $C_{4,-4}$  in (19) as

$$\xi_{4,1}^{\pm 4} = C_{4,\pm 4} d_4 = -M_0 \frac{d_4^\top}{\sqrt{\pi} d_4^\perp} (a \pm bi) c \quad (23)$$

where

$$d_4^\top = R_r^6 + \frac{9\mu_m R_b^6 R_r^9}{4(\mu_r - \mu_m) R_b^9 - (4\mu_r + 5\mu_m) R_r^9}$$

$$d_4^\perp = 5(\mu_m - 1) + \frac{9\mu_m (4\mu_r + 5\mu_m) R_r^9}{4(\mu_r - \mu_m) R_b^9 - (4\mu_r + 5\mu_m) R_r^9}.$$

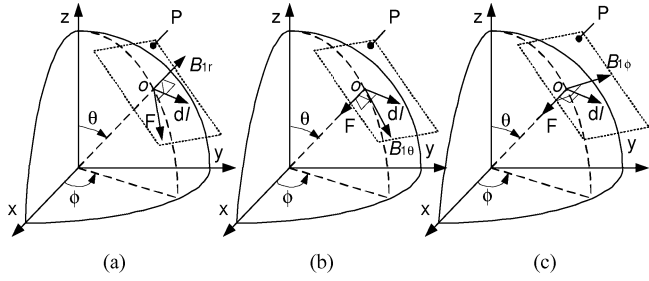


Fig. 4. Force activated by three components of the flux density (P is a plane tangential to the sphere at point O;  $dl$ ,  $B_{1\theta}$ ,  $B_{1\phi}$  are vectors on plane P;  $B_{1r}$  is normal to plane P. (a)  $r$ -direction. (b)  $\theta$ -direction. (c)  $\phi$ -direction.

3) *Solution of Magnetic Scalar Potential and Flux Density:* Substituting  $\xi_{4,1}^4$  and  $\xi_{4,1}^{-4}$  into (11) and discarding the higher order harmonic terms result in

$$\Phi_1 = M_0 \frac{3cd_4^\top}{8\pi d_4^\perp} \sqrt{\frac{35}{2}} r^{-5} \sin^4 \theta (a \cos 4\phi - b \sin 4\phi). \quad (24)$$

Using (1) and (7), the flux density in Region 1 can be obtain as

$$\begin{bmatrix} B_{1r} \\ B_{1\theta} \\ B_{1\phi} \end{bmatrix} = \frac{3\mu_0 M_0 cd_4^\top}{8\pi d_4^\perp} \sqrt{\frac{35}{2}} r^{-6} s\theta^3 \begin{bmatrix} 5s\theta(a c4\phi - b s4\phi) \\ 4c\theta(b s4\phi - a c4\phi) \\ 4(a s4\phi + b c4\phi) \end{bmatrix} \quad (25)$$

where  $s\theta$ ,  $c\theta$ ,  $s4\phi$ , and  $c4\phi$  denote  $\sin \theta$ ,  $\cos \theta$ ,  $\sin 4\phi$ , and  $\cos 4\phi$ , respectively. The direction of the force generated by each component of the flux density can be determined as shown in Fig. 4. The differential length  $dl$  of the wire is tangent to the spherical surface at point O. Note that only  $B_{1r}$  can produce a torque to change the rotor orientation.  $B_{1\theta}$  and  $B_{1\phi}$  do not produce torque on the rotor because the action lines of magnetic forces generated by  $B_{1\phi}$  and  $B_{1\theta}$  pass through the rotor center. Consequently, the following discussion focuses on the radial component  $B_{1r}$ .

#### IV. FORMULATION OF THE TORQUE MODEL

Because the stator poles are air-core coils, Lorentz force law can be employed for obtaining the torque model of this PM spherical actuator.

##### A. Approximation of Coil Geometry

To facilitate the integration of torque in spherical coordinates, we approximate the cylindrical coil denoted by ABCDA in Fig. 5 with a conical-shaped coil denoted as A'B'C'D'A'. With such approximation, the volume swept by ABCDA is about 97% of that swept by A'B'C'D'A'. Therefore, in considering the wiring on the coils, the total length of the wires wrapped around the two coil geometries are about the same. Thus, computation of the actuator torque based on Lorentz force law can be simplified with the spherical geometry of negligible differences. The sectional area of A'B'C'D'A' can be specified by four parameters:  $R_0$ , the distance from the rotor center to the top surface of the coil;  $R_1$ , the distance from the rotor center to the bottom surface

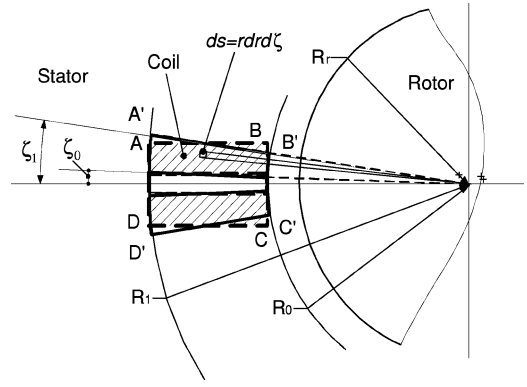


Fig. 5. Approximation of the coil shape (sectional view).

of the coil;  $\zeta_0$ , the inner surface angle of the coil; and  $\zeta_1$ , the outer surface angle of the coil.

##### B. Torque Model of a Single Coil

1) *Integral Form of Actuator Torque:* Consider a differential length  $dl$  of the winding. Fig. 5 shows the differential sectional area of  $dl$  which can be computed by  $ds = r dr d\zeta$ . The current passing through this section area is  $J_i r dr d\zeta$ , where  $J_i$  is the current density in the sectional area of the  $i$ th coil. According to Lorentz force law, the differential force on the rotor caused by the interaction between magnetic field of the rotor and current-carrying conductor  $dl$  is

$$d\mathbf{F} = -I dl \times B_{1r}(r, \theta, \phi) \mathbf{e}_r = -J_i r dr d\zeta dl \times B_{1r}(r, \theta, \phi) \mathbf{e}_r$$

where the negative sign indicates that the force imposed on the rotor by  $dl$  is the reaction force of the one exerted by the magnetic field. The torque generated is thus

$$d\mathbf{T}_i = r \mathbf{e}_r \times [-J_i r dr d\zeta dl \times B_{1r}(r, \theta, \phi) \mathbf{e}_r].$$

Integrating this differential torque within the entire volume covered by the  $i$ th coil gives the total torque produced by a single coil

$$\mathbf{T}_i = J_i \int_{R_0}^{R_1} \int_{\zeta_0}^{\zeta_1} \left\{ \int_C r \mathbf{e}_r \times [B_{1r}(r, \theta, \phi) \mathbf{e}_r \times dl] \right\} r dr d\zeta. \quad (26)$$

Note that the symbol  $\int_C$  as in (26) denotes the line integral of the differential torque along a circular loop of the winding that has a ‘‘wire’’ section area of  $ds$ . The differential length  $dl$  is perpendicular to  $\mathbf{e}_r$ . Thus, the relationship of  $\mathbf{e}_r \times (\mathbf{e}_r \times dl) = -dl$  can be readily obtained. As a result, (26) is reduced to

$$\mathbf{T}_i = -J_i \int_{R_0}^{R_1} \int_{\zeta_0}^{\zeta_1} \left\{ \int_C r B_{1r}(r, \theta, \phi) dl \right\} r dr d\zeta. \quad (27)$$

2) *Solution of the Torque Integral:* The solution to (27) is to express  $\mathbf{T}_i$  with the coil position in the rotor frame ( $\theta_i$ ,  $\phi_i$ ) and the current input  $J_i$ .

The wire loop in Fig. 6 represents one loop of winding on the sphere surface. A pair of  $\theta_i$  and  $\phi_i$  can specify the direction of

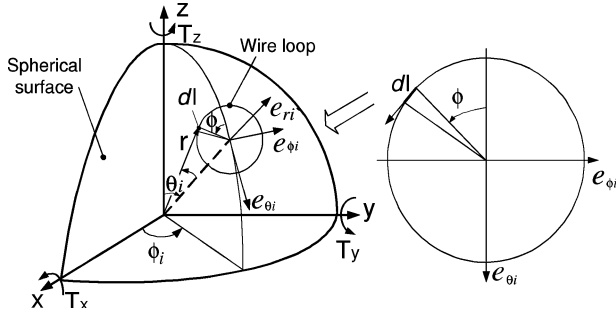


Fig. 6. One loop of wire on the sphere surface.

the  $i$ th coil axis in the rotor frame. Correspondingly,  $\mathbf{e}_{\theta_i}$  and  $\mathbf{e}_{\phi_i}$  represent the unit vectors in  $\theta_i$  and  $\phi_i$  directions. The segment  $d\mathbf{l}$  can be expressed as

$$d\mathbf{l} = r \sin \zeta d\psi (\sin \psi \mathbf{e}_{\theta_i} - \cos \psi \mathbf{e}_{\phi_i}). \quad (28)$$

Substituting  $B_{1r}$  in (25) and (28) into (27), and using the relation between Cartesian coordinates and  $\zeta, \psi, \theta_i, \phi_i$ , the expression of  $\mathbf{T}_i$  can be finally obtained as

$$\mathbf{T}_i = [T_{xi} \quad T_{yi} \quad T_{zi}]^T = T_c \mathbf{f}(\theta_i, \phi_i) J_i \quad (29)$$

where  $T_c = \sqrt{\frac{35}{2} \frac{15\mu_0 M_0 c d_4}{16\pi} (R_0^{-2} - R_1^{-2})}$ , and  $\mathbf{f}(\theta_i, \phi_i) = [f_x(\theta_i, \phi_i) \quad f_y(\theta_i, \phi_i) \quad f_z(\theta_i, \phi_i)]^T$  is a  $3 \times 1$  vector completely determined by the coils position in the rotor frame [see [18] for the expression of  $\mathbf{f}(\theta_i, \phi_i)$ ].

### C. Torque Model of the Full Set of Coils

Equation (29) represents the torque of a single coil. With  $N$  coils on the stator, there are  $N$  torque equations like (29). Arranging all  $N$  equations in a matrix form, the torque model of the spherical actuator with a complete set of coils can be obtained

$$\begin{aligned} \mathbf{T} &= T_c \begin{bmatrix} f_x(\theta_1, \phi_1) & f_x(\theta_2, \phi_2) & \cdots & f_x(\theta_N, \phi_N) \\ f_y(\theta_1, \phi_1) & f_y(\theta_2, \phi_2) & \cdots & f_y(\theta_N, \phi_N) \\ f_z(\theta_1, \phi_1) & f_z(\theta_2, \phi_2) & \cdots & f_z(\theta_N, \phi_N) \end{bmatrix} \begin{bmatrix} J_1 \\ J_2 \\ \vdots \\ J_N \end{bmatrix} \\ &= T_c \mathbf{Q} \mathbf{J} \end{aligned} \quad (30)$$

where  $\mathbf{J} = [J_1 \quad J_2 \quad \cdots \quad J_N]^T$  represents currents passing through  $N$  coils, and  $\mathbf{Q}$  is defined to be the torque matrix

$$\mathbf{Q} = \begin{bmatrix} f_x(\theta_1, \phi_1) & f_x(\theta_2, \phi_2) & \cdots & f_x(\theta_N, \phi_N) \\ f_y(\theta_1, \phi_1) & f_y(\theta_2, \phi_2) & \cdots & f_y(\theta_N, \phi_N) \\ f_z(\theta_1, \phi_1) & f_z(\theta_2, \phi_2) & \cdots & f_z(\theta_N, \phi_N) \end{bmatrix}.$$

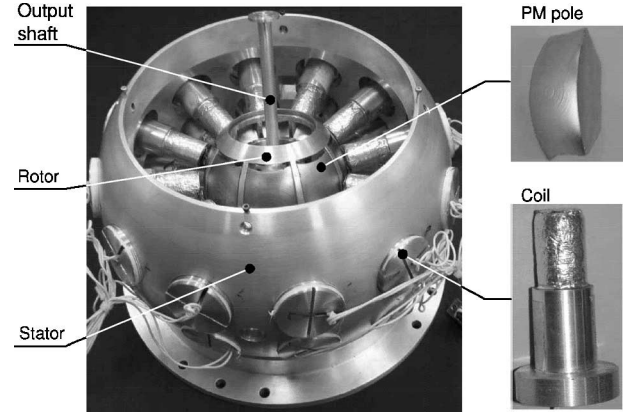


Fig. 7. Prototype of spherical actuator.

TABLE I  
STRUCTURE SPECIFICATIONS OF SPHERICAL ACTUATOR

Inner / outer stator radius	95 / 112.5 (mm)
Rotor radius	46.5 (mm)
Rotor core radius	23 (mm)
PM pole parameters	$\alpha=40^\circ, \beta=70^\circ$
Number of rotor poles (PM)	8
Number of stator poles (coil)	24 / 2 layers
Number of coil turns	1027
Maximum tilting angle	$\pm 11^\circ$
Maximal spinning torque	4 (N·m)
Maximal tilting torque	0.8 (N·m)

## V. PROTOTYPE AND EXPERIMENTS

### A. Prototype

A research prototype of the actuator has been developed as shown in Fig. 7. The specification is listed in Table I. The large size of stator (aluminum) is to facilitate the experimental research and the eddy current. The diameter of the aluminum coil core is about 3 mm. The use of aluminum for the coil core and stator is undesirable for high dynamic performance. By using nonmetal material such as Delrin in future designs, the eddy current effect and the stator size can be reduced. A conical-shaped coil will be designed to increase the winding turns and actuator torque. The maximum torque in the table is obtained with a 3-A current input. Although the maximum tilting torque is much smaller than the maximum spinning torque, a rotor with two-layer PM poles has been proposed recently to achieve similar values of spinning and tilting torques. A spherical bearing that can achieve 3-DOF rotation is assembled at the rotor center to support the rotor. It avoids the wear of rotor and friction torque

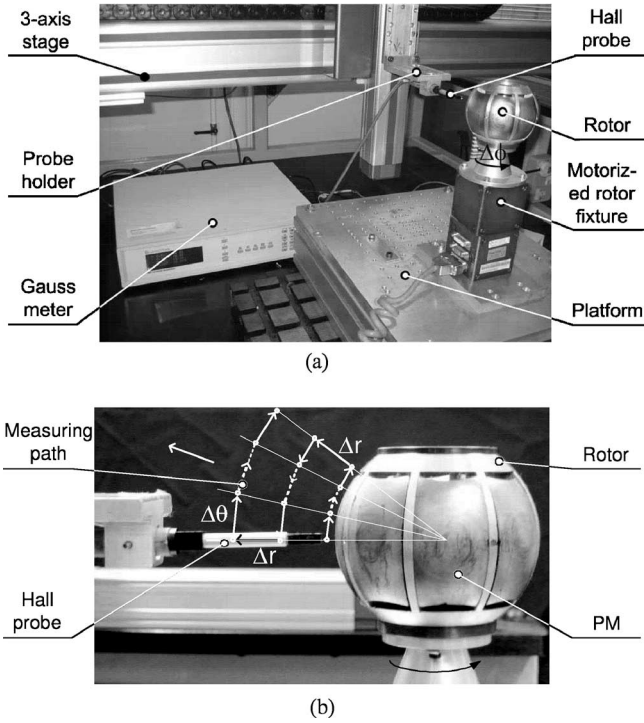


Fig. 8. Measurement of flux density. (a) Testbed. (b) Measuring plane.

produced by contact bearings. This configuration allows more coils to be incorporated into the stator so that the maximum tilting angle can be increased up to  $\pm 45^\circ$  and the resolution can also be improved. By using this prototype, experiments on magnetic field and torque variation can be carried out.

### B. Experiment on Magnetic Field

1) *Testbed and Measuring Process:* The flux density  $\mathbf{B}$  is a 3-D vector, not a scalar. Therefore, it is necessary to measure all three components of the flux density vector at any measuring point surrounding the rotor. A three-axis Hall probe is employed in this measurement. Fig. 8(a) shows the complete flux density measurement testbed. The Hall probe is mounted on a high-precision three-axis translational motion stage so that it can pinpoint to any location near the rotor. It is also connected to the Gauss meter to display the measured flux density in three components. The Gauss meter is linked to a personal computer (PC) through a data-acquisition card. The measured flux density then can be automatically stored on the PC. The rotor is mounted on a motorized fixture that can spin along the rotor axis in  $360^\circ$ . Thus, it is possible to measure the magnetic flux density in the longitudinal direction of the rotor by simply rotating the rotor using the fixture without reorienting the Hall probe.

The Hall probe moves along a predetermined path illustrated in Fig. 8(b) and takes measurement of flux density at sampling points along the path. As the rotor structure is symmetric about the equatorial plane, the measurement is only carried out for the upper hemisphere. The measuring path starts from a point along the center axis of a PM pole and very close to the ro-

tor surface. The measuring path is kept along a vertical plane called a *measuring plane*. The probe moves along an arc upwards on the plane while keeping a constant normal distance  $d_a$  with the rotor surface. It can be seen from Fig. 8(b) that the neighboring sampling points keep a constant angle of  $\Delta\theta$  with respect to the rotor center. After the probe completes an arc of  $\theta = 30^\circ$ , the probe offsets a distance of  $\Delta r$  radially and then carries out measurement along the subsequent arc path. This measuring process is repeated with increasing radial distance  $r$  until the flux density is significantly small. For our measurement, the maximum motion in the  $r$ -direction is 30 mm. This distance far exceeds the possible location of the stator coil. Due to the constant-angle sampling pattern, the measuring points are sparsely located when the radius  $r$  increases. It is coincident with the fact that the gradient of the flux density decreases with the increase of  $r$ . Therefore, this sampling method is more effective than sampling with equal distance points, which requires more sampling points.

After completion of the measurement task in one measuring plane, the PC sends commands to the controller of rotor fixture to turn the rotor with an angle of  $\Delta\phi$ . The Hall probe is thus positioned in a new measuring plane and the same data acquisition procedure is repeated. The entire process of positioning the probe, taking measurement, and turning the rotor can be fully automated.

2) *Experimental Result:* In our prototype actuator, PM poles with  $B_{rem} = 1.0$  T are used. Comparisons between experimental result and analytical model are presented in Fig. 9. Fig. 9(a) shows the distribution of  $B_{1r}$  along the longitudinal ( $\phi$ ) and latitudinal ( $\theta$ ) directions ( $\theta = 75^\circ \sim 90^\circ$ ,  $\phi = 0^\circ \sim 360^\circ$ ) at a fixed radial distance  $d_a$ . The analytical and experimental results of the flux density  $B_{1r}$  are approximately the same. To observe the difference of the two results, Fig. 9(b) is used to show the variation of  $B_{1r}$  along the rotor equator ( $\theta = 90^\circ$ ). It can be seen from Fig. 9(a) and (b) that the experimental measurement fits the analytical result well. Along the rotor equator, i.e., the  $\phi$ -direction, eight positive/negative peaks can be observed due to eight alternately magnetized PM poles. The maximum difference between the experimental data and analytical model occurs along the rotor equator and in between two rotor poles (300 G or 5% of the measured data). This indicates that the accuracy of the proposed magnetic field model is acceptable. With the inclusion of high-order harmonics in the magnetic field model, the difference may be reduced.

### C. Experiment on Actuator Torque

1) *Torque Generated by a Single Coil:* The objective of this experiment is to verify the torque generated by a single coil as described in (29). A testbed is developed for the measurement of the force/torque generated between the PM rotor and a single coil as shown in Fig. 10. The coil is supplied by a dc power (Topward 3303D). A six-axis force/torque sensor (ATI Nano43) is mounted on the shaft of the rotor which in turn is connected to a guide shaft. This guide shaft can slide along the slot of the arc guide so that a tilting motion of the rotor is able to be achieved. In addition, the guide shaft can rotate about its

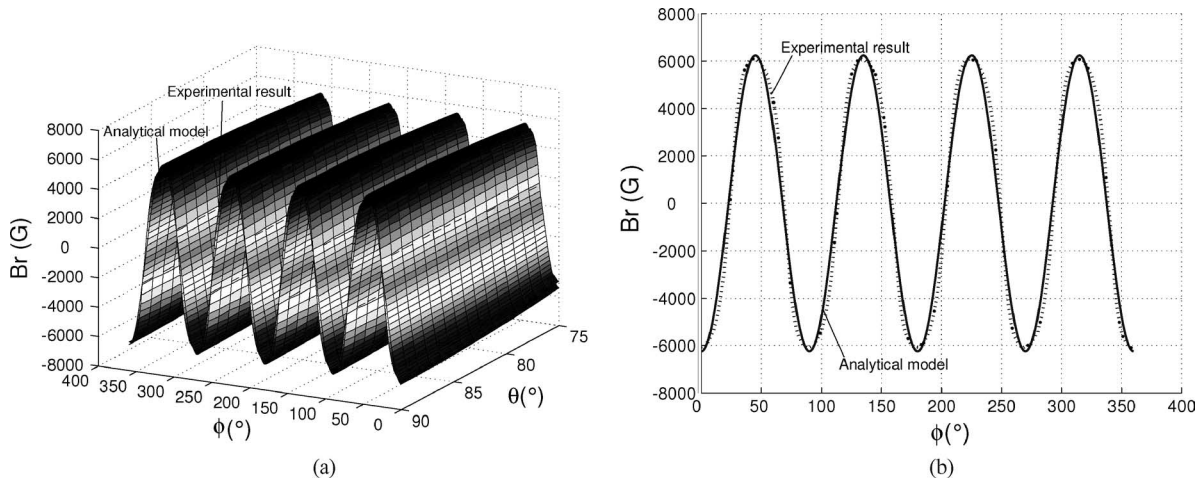


Fig. 9. Comparison of experimental result and analytical model ( $B_r$ ). (a) 3D view of experimental versus analytical results ( $d_a = 0.5$  mm). (b) 2D view of experimental versus analytical results ( $\theta = 90^\circ$ ).

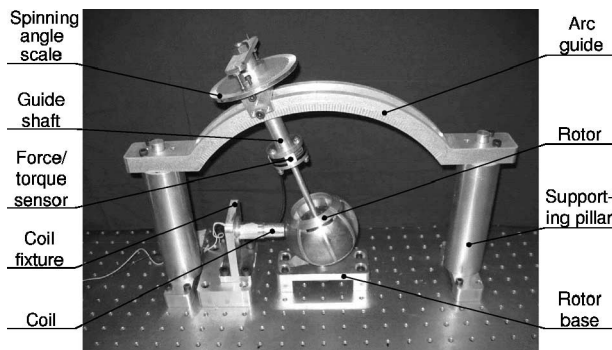


Fig. 10. Testbed for force/torque measurement of single coil.

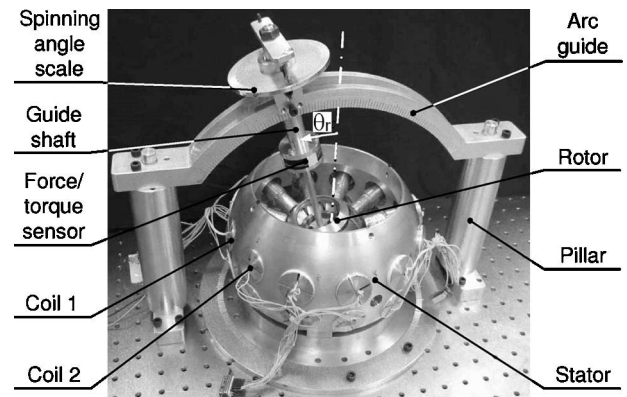


Fig. 11. Force/torque measurement on two coils.

own axis along with the rotor. The tilting motion and rotation can provide the values of  $\theta$  and  $\phi$ , which specify the position of the coil axis in the rotor frame. By using this testbed, the force/torque variation between the rotor and the coil with respect to  $\theta$  and  $\phi$  can be obtained. In this experiment, the measuring range of  $\phi$  is from  $0^\circ$  to  $360^\circ$ , whereas the measuring range of  $\theta$  is from  $70^\circ$  to  $110^\circ$ , which cover the range of coils on the stator. The torque is a 3-D vector with components  $T_x$ ,  $T_y$ , and  $T_z$  defined on the rotor frame. The torque vector is pose  $(\theta, \phi)$  dependant, where  $\theta$  and  $\phi$  specify the coil-axis orientation in the rotor frame. The variation of torque components can be visualized as a surface with respect to  $(\theta, \phi)$ . Fig. 12 presents the torque variation of experimental and analytical results. In the experiment, 3-A current is supplied to the coil. The change of  $T_y$  is the same as  $T_x$  with  $30^\circ$  shift in the  $\phi$ -direction. It can be seen that the analytical model fits the experimental result well with maximum difference of 8% of the experimental result. Adding in high-order terms may improve the accuracy of the torque model further.

2) *Torque Generated by Multiple Coils (Two Coils)*: According to (30), the total torque of the spherical actuator is the

superposition of torques generated by individual coils. The objective of this experiment is to verify the superposition principle of the spherical actuator torque. The testbed of this experiment is the same as that in Fig. 10 except that the stator is used to replace the single coil. To verify the superposition principle, force/torque measurement is conducted on two arbitrarily chosen coils indicated in Fig. 11. The initial positions of these coils in the rotor frame are  $(\theta = 79^\circ, \phi = 0)$  and  $(\theta = 79^\circ, \phi = 30^\circ)$ . In this experiment, the rotor shaft changes the orientation by sliding along the arc guide with an angle  $\theta_r$ . For any specified rotor orientations, three sets of data are captured: torque produced by energizing Coil 1 alone, by Coil 2 alone, and by Coil 1 and 2 simultaneously. By comparing the vector sum of the first two sets of torque values with the last set, the superposition of actuator torque can be evaluated. It can be seen from Fig. 13(a)–(c) that the superposition of torque generated by two individual coils fits well with the torque generated by energizing two coils simultaneously. Hence, the linear model of (30) can be used for the spherical actuator.

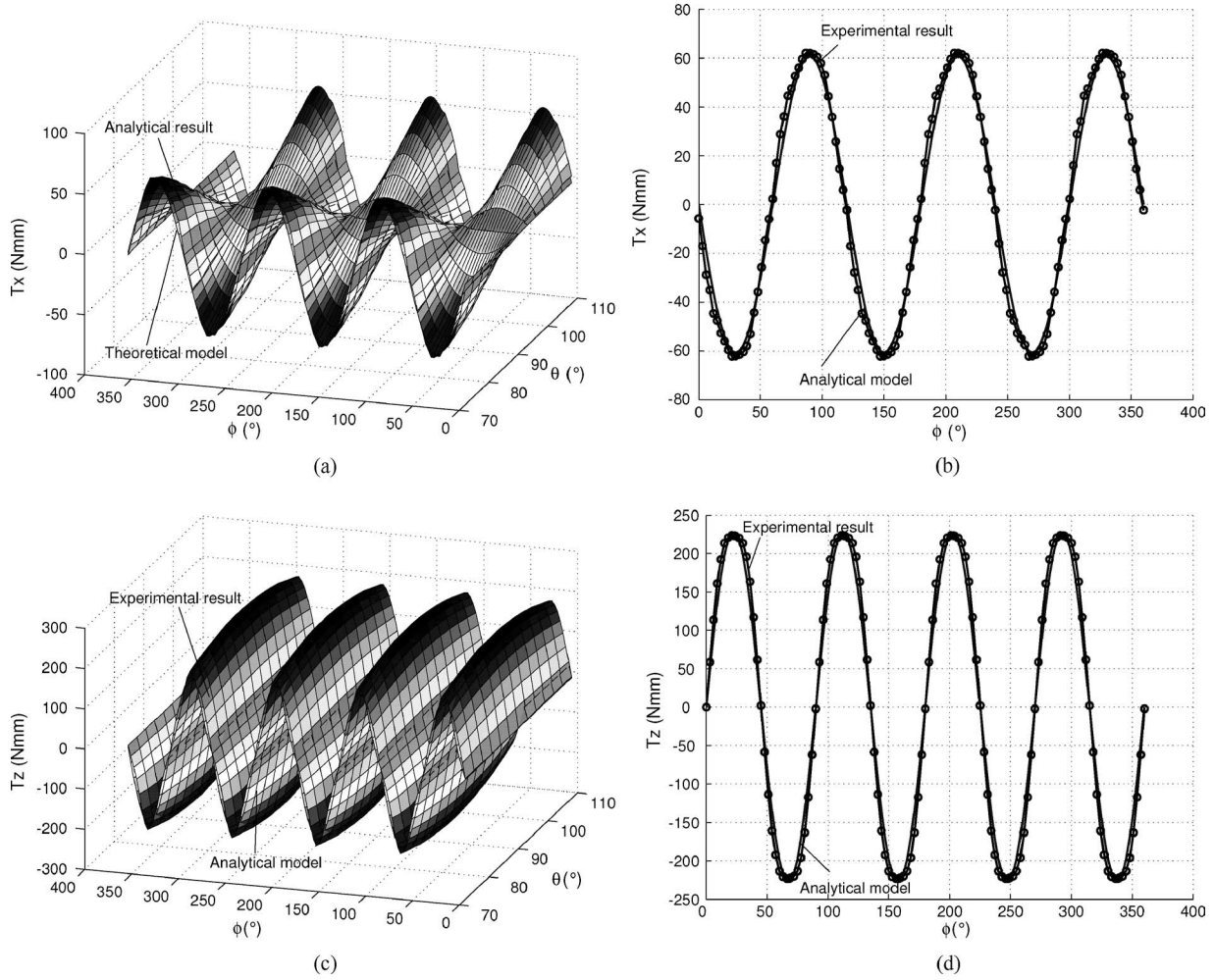


Fig. 12. Analytical versus experimental results of torque generated by single coil (a) Analytical versus experimental results in 3-D space ( $T_x$ ) (b) Analytical versus experimental results in 2-D ( $T_x, \theta = 72^\circ$ ) (c) Analytical versus experimental results in 3-D space ( $T_z$ ) (d) Analytical versus experimental results in 2-D ( $T_z, \theta = 90^\circ$ ).

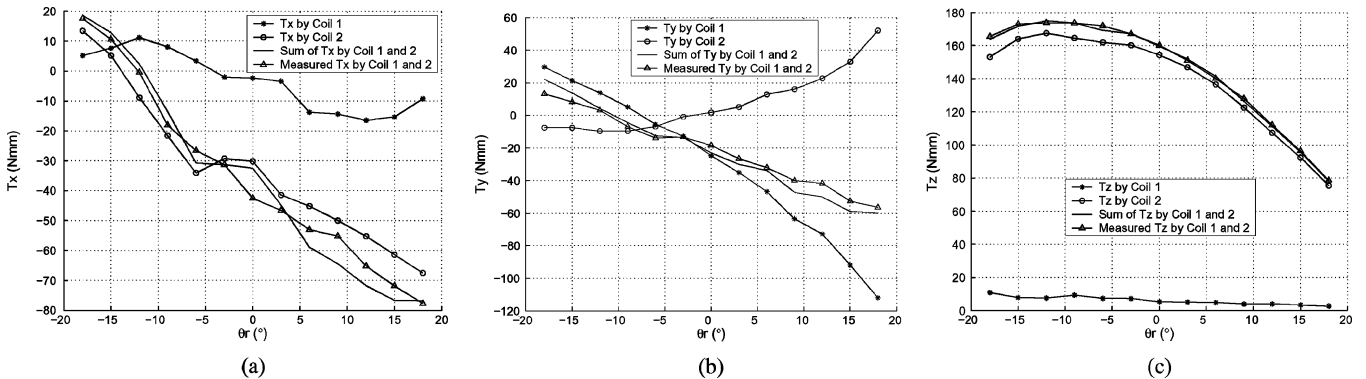


Fig. 13. Superposition of actuator torque. (a) Torque x. (b) Torque y. (c) Torque z.

3) *Linearity of Torque Model*: According to (29) and (30), the torque output is proportional to the current input. Experiments are carried out to verify this relation. The coil is fixed at an arbitrary position in the rotor frame, such as  $\phi = 21^\circ, \theta = -9^\circ$ . By varying the current input, torque outputs are measured.

Fig. 14 shows the experimental and theoretical results. According to these results, three components of the torque are all proportional to the current input. This linear property will facilitate the real-time position and velocity control of the actuator.

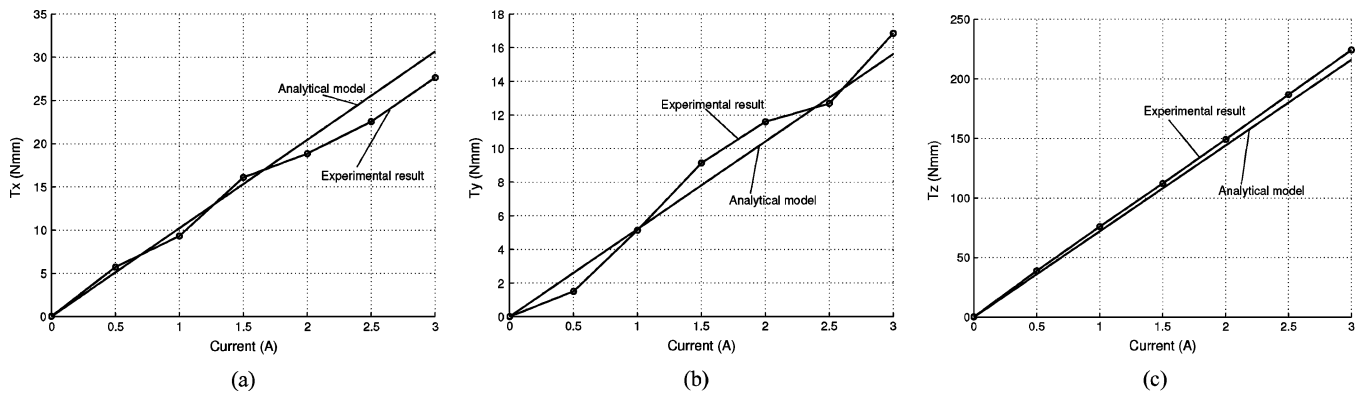


Fig. 14. Linear relation between actuator torque and current input. (a) Torque  $x$ . (b) Torque  $y$ . (c) Torque  $z$ .

## VI. CONCLUSION

This paper presented the development of an analytical expression of the output torque for a 3-DOF spherical actuator in terms of input currents to the coils. Two major works were crucial to the derivation of the torque model: 1) formulation of the analytical magnetic field distribution of the PM rotor based on Laplace's equation with suitable boundary conditions, and 2) superposition of the motor torque produced by the input current to multiple stator coils according to Lorentz force law. Experimental verification of the analytical 3-D magnetic field surrounding the rotor and 3-D actuator torques was carried out. The tasks included the design and installation of a semiautomatic 3-D magnetic field measurement system and 3-D torque measurement testbed, measurement data acquisition, and processing. Comparisons between analytical and experimental data have shown consistency of the proposed magnetic field model of the rotor and torque model although there are minor errors which may be due to the omission of the higher order terms of the harmonics. The analytical expression of the actuator torque facilitates the real-time control of the spherical actuator as a servo system for precision applications. Design optimization on the actuator dimensions and arrangement of the PM poles and stator coils hence becomes possible.

## ACKNOWLEDGMENT

The authors would like to acknowledge assistance from Dr. L. Wei, C. K. Lim, J. Su, Dr. W. Chen, and T. Thng.

## REFERENCES

- [1] F. C. Williams, E. R. Laithwaite, and J. Eastham, "Development and design of spherical induction motors," *Proc. Inst. Elect. Eng.*, vol. 106, no. 3036U, pp. 471–487, Dec. 1959.
- [2] K. Davey, G. Vachtsevanos, and R. Powers, "The analysis of fields and torques in spherical induction motors," *IEEE Trans. Magn.*, vol. 23, no. 1, pp. 273–282, Jan. 1987.
- [3] G. J. Vachtsevanos, K. Davey, and K. M. Lee, "Development of a novel intelligent robotic manipulator," *IEEE Contr. Syst. Magn.*, vol. 7, no. 3, pp. 9–15, Jun. 1987.
- [4] K. M. Lee and C. K. Kwan, "Design concept development of a spherical stepper for robotic applications," *IEEE Trans. Robot. Autom.*, vol. 7, no. 1, pp. 175–181, Feb. 1991.
- [5] K. M. Lee, R. B. Roth, and Z. Zhou, "Dynamic modeling and control of a ball-joint-like variable-reluctance spherical motor," *ASME J. Dyn. Syst., Meas., Contr.*, vol. 118, pp. 29–40, Mar. 1996.
- [6] Z. Zhou and K. M. Lee, "Characterization of a three degrees-of-freedom variable-reluctance spherical motor," *J. Syst. Eng.*, vol. 4, pp. 60–69, 1994.
- [7] K. M. Lee, R. A. Sosseh, and Z. Wei, "Effects of the torque model on the control of a VR spherical motor," *Control Eng. Practice*, vol. 12/11, pp. 1437–1449, 2004.
- [8] J. Wang, G. W. Jewell, and D. Howe, "Analysis, design and control of a novel spherical permanent-magnet actuator," in *Proc. IEE Elect. Power Appl.*, vol. 145, no. 1, Jan. 1998, pp. 61–71.
- [9] W. Wang, J. Wang, G. W. Jewell, and D. Howe, "Design and control of a novel spherical permanent magnet actuator with three degrees of freedom," *IEEE/ASME Trans. Mech.*, vol. 8, no. 4, pp. 457–468, Dec. 2003.
- [10] J. Wang, G. W. Jewell, and D. Howe, "A novel spherical actuator: design and control," *IEEE Trans. Magn.*, vol. 33, no. 5, pp. 4209–4211, Sep. 1997.
- [11] —, "A novel spherical actuator with three degrees-of-freedom," in *IEEE Trans. Magn.*, Jun. 1998, vol. 34, pp. 2078–2080.
- [12] G. S. Chirikjian and D. Stein, "Kinematic design and commutation of a spherical stepper motor," *IEEE/ASME Trans. Mech.*, vol. 4, no. 4, pp. 342–353, Dec. 1999.
- [13] K. Kahlen, I. Voss, C. Priebe, and R. W. D. De Doncker, "Torque control of a spherical machine with variable pole pitch," *IEEE Trans. Power Electron.*, vol. 19, no. 6, pp. 1628–1634, Nov. 2004.
- [14] K. M. Lee, H. Son, and J. Joni, "Concept development and design of a spherical wheel motor (SWM)," in *Proc. IEEE/ASME Int. Conf. Robot. Automation*, Monterey, CA, Jul. 2005, pp. 335–340.
- [15] K. M. Lee and H. Son, "Torque model for design and control of a spherical wheel motor," in *Proc. IEEE/ASME Int. Conf. Adv. Intelligent Mech.*, Monterey, CA, Jul. 2005, pp. 335–340.
- [16] L. Yan, I. M. Chen, C. K. Lim, G. L. Yang, W. Lin, and K. M. Lee, "Experimental investigation on the magnetic field of a permanent magnet spherical actuator," in *Proc. IEEE/ASME Int. Conf. Adv. Intelligent Mech.*, CA, Jul. 2005, pp. 341–346.
- [17] C. K. Lim, I. M. Chen, L. Yan, G. L. Yang, W. Lin, and K. M. Lee, "Design & analysis of a new variable stator pole for a dc spherical actuator," in *Proc. IEEE/ASME Int. Conf. Adv. Intelligent Mech.*, California, USA, Jul. 2005, pp. 347–352.
- [18] L. Yan, I. M. Chen, C. K. Lim, G. L. Yang, W. Lin, and K. M. Lee, "Torque modeling of a spherical actuator based on lorentz force law," in *Proc. IEEE Int. Conf. Robot. Automation*, Barcelona, Spain, Apr. 2005, pp. 3657–3662.



**Liang Yan** received the B.Eng. degree from North China Institute of Technology, Taiyuan, Shanxi, China, the M.Eng. degree from Beijing Institute of Technology (BIT), Beijing, China, in 1995 and 1998, respectively. Currently, he is working toward the Ph.D. degree in Nanyang Technological University, Singapore.

His research interests include electromagnetic actuators, sensors, navigation system, modeling and design of mechanical system, system assembly, and expert system design.

Mr. Yan was the recipient of the National Defense Science and Technology Award of China in 2002.



**I-Ming Chen** (M'95–SM'06) received the B.S. degree from the National Taiwan University, Taipei, Taiwan, in 1986, and the M.S. and the Ph.D. degrees from the California Institute of Technology, Pasadena, in 1989 and 1994, respectively.

Since 1995, he has been with the School of Mechanical and Aerospace Engineering of Nanyang Technological University, Singapore. In 1999, he was JSPS Visiting Scholar at Kyoto University, Japan. In 2004, he was a Visiting Scholar in the Department of Mechanical Engineering of Massachusetts Institute of Technology (MIT), Cambridge. He is also the Adjunct Professor with Xian Jiao Tong University, Xian, China. He is the author of more than 130 technical articles in refereed international journals and conferences. His research interests include reconfigurable automation, biomedical applications of reconfigurable robotic systems, parallel kinematics machines (PKM), biomorphic underwater robots, and smart material-based actuators.

Dr. Chen is a Fellow of the Singapore-MIT Alliance under the Manufacturing Systems and Technology (MST) Program. He is serving on the editorial boards of IEEE/ASME TRANSACTIONS ON MECHATRONICS, *Robotica-International Journal*, and the steering committee of CISM-IFTOMM Symposium on Robot Design, Dynamics and Control (ROMANSY). He is also General Chairman of the 2009 IEEE/ASME International Conference on Advanced Intelligent Mechatronics (AIM2009) in Singapore. He is a Member of ASME, Chairman of the Prototyping for Robotics and Automation Technical Committee under IEEE Robotics and Automation Society, and a Member of the RoboCup Singapore National Committee.



**Guilin Yang** (M'02) received the B.Eng. and the M.Eng. degrees from the Jilin University of Technology (now Jilin University), Changchun, China, in 1985 and 1988, respectively, and the Ph.D. degree from Nanyang Technological University, Singapore, in 1999.

In 1988, he joined the School of Mechanical Engineering, Shijiazhuang Railway Institute, Hebei, China, as a Lecturer, and was a Division Head and then the Vice Dean of the school for nearly seven years. Currently, he is a Research Scientist and the Deputy Group Manager of the Mechanics Group, Singapore Institute of Manufacturing Technology, Singapore. He is the author of over 100 technical papers published in refereed international journals and conferences. His current research interests include computational kinematics, multi-body dynamics, parallel-kinematics machines, modular robots, flexure-based precision mechanisms, electromagnetic actuators, rehabilitation devices, and industrial robot systems.

Dr. Yang is a Technical Committee Member of Robotics of International Federation for the Promotion of Mechanism and Machine Science and the Secretary of the Singapore Chapter of the IEEE Robotics and Automation Society.



**Kok-Meng Lee** (M'89–SM'02–F'05) received the B.S. degree from the State University of New York, Buffalo, in 1980, and the S.M. and Ph.D. degrees from the Massachusetts Institute of Technology, Cambridge, in 1982 and 1985, respectively.

Currently, he is a Professor at the Woodruff School of Mechanical Engineering at the Georgia Institute of Technology, Atlanta. He is the holder of eight patents in machine vision, 3-DOF spherical motor/encoder, and live-bird handling system. His research interests include system dynamics/control, robotics, automation, and mechatronics.

Dr. Lee is a Fellow of ASME. He was the recipient of the National Science Foundation (NSF) Presidential Young Investigator, Sigma Xi Junior Faculty Research, International Hall of Fame New Technology, and Kayamori Best Paper awards.

Dr. Lee is a Fellow of ASME. He was the recipient of the National Science Foundation (NSF) Presidential Young Investigator, Sigma Xi Junior Faculty Research, International Hall of Fame New Technology, and Kayamori Best Paper awards.